



LAWRENCE
LIVERMORE
NATIONAL
LABORATORY

Wire-based Additive Manufacturing of Stainless Steel Components

J. W. Elmer, J. Vaja, J. S. Carpenter, D. R. Coughlin, M.
J. Dvornak, P. Hochanadel, P. Gurung, A. Johnson, G.
Gibbs

April 10, 2019

The Welding Journal

Disclaimer

This document was prepared as an account of work sponsored by an agency of the United States government. Neither the United States government nor Lawrence Livermore National Security, LLC, nor any of their employees makes any warranty, expressed or implied, or assumes any legal liability or responsibility for the accuracy, completeness, or usefulness of any information, apparatus, product, or process disclosed, or represents that its use would not infringe privately owned rights. Reference herein to any specific commercial product, process, or service by trade name, trademark, manufacturer, or otherwise does not necessarily constitute or imply its endorsement, recommendation, or favoring by the United States government or Lawrence Livermore National Security, LLC. The views and opinions of authors expressed herein do not necessarily state or reflect those of the United States government or Lawrence Livermore National Security, LLC, and shall not be used for advertising or product endorsement purposes.

Wire-based Additive Manufacturing of Stainless Steel Components

John W. Elmer¹, Jay Vaja², John S. Carpenter³, Daniel R. Coughlin³, Matthew J. Dvornak³, Pat Hochanadel³, Parogya Gurung², Andy Johnson², and Gordon Gibbs¹

¹Lawrence Livermore National Laboratory, ²Los Alamos National Laboratory, ³Aldermaston Weapons Establishment

Subtitle

Laser, arc, and electron beam sources were compared for freeform fabrication of metal parts at high deposition rates

Keywords

Wire-fed AM, high deposition rate AM, laser AM, wire-arc AM, electron beam AM, stainless steels, welding, mechanical properties, anisotropy, grain texture, chemical composition, heat input, freeform fabrication, layer by layer fabrication.

Abstract

Three different wire-fed additive manufacturing (AM) processes were employed to evaluate differences between laser, arc, and electron beam heat sources used for high deposition rate AM on the order of 1 kg/hr. Optimum weld and build parameters were developed independently to match the characteristics of each heat source, using 308L stainless steel wire as the feed stock. Laser-wire AM was made with the lowest energy per unit length of weld and had the best control of the melt pool and surface finish. Wire-arc based AM had an intermediate energy per unit length of weld of approximately 5x that of the laser process, while electron beam wire AM had the highest energy per unit length of weld at approximately 10x that of the laser process. Analysis of the parts that were built included evaluation of mechanical properties and microstructures, and these properties are discussed with respect to the difference in input energy and cooling rates. Results show that all three processes build parts with properties that exceed those of annealed 304L wrought stainless steel. However significant differences exist between the processes, and the results presented here can be used to help select the best wire-fed process for a given high deposition rate application.

Introduction

Wire-based additive manufacturing represents three of the four processes used to additively manufacture parts at high deposition rates (HDR). The three wire-based processes use either electron beam, laser beam, or arc heat sources to melt a wire feed stock, while the fourth HDR process uses directed powders and laser heat sources¹⁻⁴. HDR additive manufacturing (AM) processes tend to use kilowatt or higher power levels, and can fabricate near net shaped parts at kg or multi kg/hr build rates with economic advantages over other AM methods⁵. These processes are distinguished from powder bed AM processes in that they are not confined to a box of prescribed dimensions, they have much higher deposition rates, they have little or no restriction in component size, and they are more economical in terms of cost per amount of material deposited¹⁻⁵. Just like powder bed processes, wire-based AM can produce thin wall, thick wall, solid, and/or cast like components without the need for a die, but with less precision due to the larger amount of material deposited per unit time. Nearly 100% of the wire is incorporated into the final part, making wire fed technologies much more efficient than powder based processes⁴. Components produced by wire-based AM can be compared to castings, but the microstructures are more refined than castings of similar size due to the fact that the AM liquid melt pool is typically only a few mm in diameter and is often orders of magnitude smaller than the finished part. The refined wire-based AM microstructures have smaller grains, less micro- and macro-segregation, and typically have better mechanical properties than castings^{1,2,4}. In addition, wire-based AM can be used to build onto, or modify, existing parts through cladding and hardfacing, and can also perform repair and maintenance of castings and other metal parts¹⁻⁴.

The three wire-based AM processes are known by different names in the literature¹⁻³, and will be referred to here as wire fed laser AM (LAM-W), wire arc additive manufacturing (WAAM), and wire fed electron beam AM (EBAM-W⁶). Each process uses a different power source, and each has advantages and disadvantages in terms of equipment and operating costs, microstructural control, heat input, surface finish of the part being made, and exposure to atmospheric contamination. Parts produced by the wire-based AM processes have the same nominal composition as the wire being used, with only minor variations in the composition due to different evaporation rates from the liquid weld pool of the various elements in the alloy⁷ or pickup of atmospheric contaminants^{8,9}.

LAM-W is a directed energy deposition method that couples conventional pulsed¹⁰ or continuous wave^{11,12} high power laser sources with CNC machines and wire feeders to produce 3D parts layer by layer without the need of a mold⁴. Wire sources can be cold or heated and are fed either coaxially^{13,14} or from the side^{4,11,12} to add metal to the weld pool, and inert gas is used to help minimize interaction of the hot metal with the atmosphere. Lasers are high energy density heat sources that can be focused to small spot sizes and positioned with high accuracy. In this process, the laser heat source is used to create a molten melt pool while the wire is fed into this pool to add metal. Small laser spot sizes and low powers allow the LAM-W process to be operated with fine wire sizes that enables parts to be produced with higher resolution than the other two wire-based AM processes. For reactive metals such as titanium, simple localized gas shielding often used with the LAM-W is insufficient to prevent oxidation and for such

materials more extended area shielding is required ¹⁵. Laser associated hazards and capital equipment costs make LAM-W a moderately high cost process to operate per amount of metal deposited.

WAAM is a freeform fabrication method that uses conventional wire-fed arc or plasma welding sources and modern robotic or CNC motion systems to produce 3D metal or alloy parts without a mold, but with less precision than the LAM-W process. WAAM can be used with plasma arc, gas tungsten arc, or gas metal arc heat sources ⁴. In the plasma arc and gas tungsten arc processes, the heat sources are used to create a melt pool and the wire is fed independently into the melt pool to add filler metal to the build, much the same as LAM-W. This has the advantage of decoupling the wire feed from the arc power, but makes wire feeding more complicated since the wire must enter the weld pool at an angle to the torch. In the gas metal arc (GMA) processes, a coaxial wire is fed through the center of the torch and is an active element of the electrical circuit being directly coupled to the input power to the arc. GMA is the easiest heat source to implement with WAAM because of its coaxial nature and routine adaptation to CNC and robotic control systems, but it does not have the flexibility that independent control of the wire feed rate of the other arc heat sources. WAAM is the least expensive of the three wire-fed processes due to the relatively low cost of the robotic systems and conventional arc welding power supplies. In addition the energy utilization of arc-based AM is typically over 90%, which far exceeds that of laser and electron beam wire-based processes ⁴. However, contact between the hot metal parts being built and the surrounding atmosphere can result in unwanted oxygen or nitrogen contamination. Such contamination can adversely affect the resulting mechanical properties of the build in oxygen sensitive metals and alloys such as titanium ^{8,9,16-18}. Handling such alloys requires special inert gas shielding considerations that increase the cost of the system, but can achieve near wire compositions of the build with moderate inert gas purge conditions ⁹.

EBAM-W is a directed energy deposition method that couples conventional electron beam welding equipment with a wire feeder, a stationary or movable electron beam gun, and additional CNC motion systems situated within the electron beam vacuum chamber to produce AM parts ^{4,19,20}. Like lasers, electron beams are high energy density heat sources that can focus its energy to small spot sizes, and has similar advantages. However, EBAM-W has one central beam that prohibits the wire from being fed coaxially with the beam. Because of this the wire is fed at an angle to the beam, which creates limitations on the direction and orientation of the gun relative to the part being built. Being in vacuum, EBAM-W does not require any special gas shielding and produces parts with no chance of picking up unwanted contaminants. This is a big advantage but vacuum chambers become large to include wire feeding and motion systems, which makes it the most expensive wire fed process in terms of capital equipment and operating costs. Being in vacuum, the parts cool more slowly than the other two processes and cannot be actively cooled through external convective inert gas. This makes the EBAM-W melt pool more difficult to control from layer to layer and more difficult to produce fine details. In addition, the microstructures created will tend to be coarser and more annealed, and the total build time will be increased relative to the other two processes.

This study comprises a collaboration between the different facilities to evaluate the microstructure and mechanical properties of parts built using the three different wire fed process. WAAM parts were built at Lawrence Livermore National Laboratory using a robotically positioned GMA heat source, LAM-W parts were built through the Aldermaston Weapons Establishment, and EBAM-W parts were built by Los Alamos National Laboratory. Similar sized rectangular bricks weighing about 5 kg each, were made by each process from 308L stainless steel wire. The resulting builds were characterized to compare build parameters and evaluate microstructure, composition, and tensile properties along different orientations relative to the AM build geometry. Results from this study are useful for comparing relative advantages and disadvantages of each process.

Experimental Methods

Laser Wire Additive Manufacturing

The LAM-W samples were produced by Laserline under subcontract to the Aldermaston Weapons Establishment (AWE)²¹, using an LDF 5000-30 laser with a Fraunhofer co-axial wire feed head. The equipment, shown in Fig. 1, features an optical setup where the collimated laser beam is split into three separate beams that subsequently converge onto the wire at a circular focal point. The setup is such that the wire is fed exactly onto the central axis of the converging laser beams, thereby creating a melt pool independent of the weld direction or gravity. Figure 1a shows the brick at an intermediate stage of completion, and Figure 1b shows the completed brick. LAM-W was used with a 1.1 mm diameter 308L stainless steel wire having the composition shown in Table 1 to build a 115x65x40 mm brick onto a 25mm thick 304L stainless steel substrate. Note that 308L SS has a similar composition to 304L SS and is readily available in 1.1 mm diameter welding wire but is not available in other forms, hence 304L was used as the starting build plate.

The LAM-W builds were made at a weld travel speed of 1.2 m/min, which is nearly 4x the speed of the WAAM builds. The remaining build and welding parameter data are summarized in Table 2 for a laser spot size of 2mm diameter. The brick was built with the deposition strategy that altered the direction of travel between passes using nearly 50% overlap of 1.4 mm for the 3 mm wide weld beads. At the end of each layer, the laser was returned to the initial starting position, and then offset 1.0 mm upward, which was then used as the starting point on the next layer. The laser was constantly powered through the entire build stage. To avoid overheating of pad, the laser power was reduced from a starting power of 1600W to 1200W. A 200W reduction in power was applied in two stages, first after the 3rd layer and one after the 6th layer. Note that the power and energy calculations presented in Table 2 assume the average laser power of 1400W. The final brick consisted of 45 layers, had a maximum deposition rate of 0.7 kg/hr and was made at an energy per unit length of 70 J/mm.

Wire Arc Additive Manufacturing

Wire arc additive manufacturing was performed using an 8-axis robotic welder to fabricate

shapes from 1.1 mm 308L stainless steel wire having the composition listed in Table 1. The robotic cell with a Fronius CMT GMAW power supply and torch are shown in Fig. 2a. This setup was used to fabricate a 130x80x95 mm solid brick built on 1-inch thick 304L stainless steel base plate as shown in Fig. 2b after wire brushing to remove the welding soot. The welding parameters are summarized in Table 2, consisting of a constant wire feed speed of 3.8 m/min, an average welding voltage of approximately 18V and current of 110A, which is about $\frac{1}{2}$ the maximum level of the power supply. The power supply was run in pulsed-CMT mode using Ar-29.5%He-0.5%CO₂ trimix shielding gas at 30 CFH flow rate through the torch. Cooling between layers used a side shield of argon gas flowing at 40 CFH while the brick rotated at a constant speed.

The WAAM builds were made at a weld travel speed of 0.32 m/min, which produced a melt pool approximately 9 mm diameter. A layer-by-layer dam-and-fill procedure was used to create the brick shape with straight edges whereby a frame is first made to define the perimeter of the brick, and then the inside of the frame was filled using a serpentine pattern with a bead overlap of approximately 50%. At the completion of each layer, argon gas was blown onto the brick for approximately 1 min. to help cool the brick. In addition, wire brushing after each layer was performed to clean the surface to minimize entrapment of surface oxides during the build. A total of approximately 5 minutes of welding time and 5 minutes of cooling/cleaning time was required per layer. The brick consisted of 40 layers at 2.3 mm offset height per layer. The build was made with a deposition rate of 1.7 kg/hr if the weld was run continuously, and was made at an energy per unit length of 371J/mm. This energy per length of weld is approximately 5x that of the LAM-W build, largely due to its lower speed, and produced larger resulting melt pools.

Electron Beam Wire Additive Manufacturing

EBAM-W builds were made on a Sciaky low voltage system (60KV maximum) using 308L stainless steel wire with the composition listed in Table 1. The system is shown in Fig. 3a and employed 1.5 mm diameter wire to make a 110x110x40 mm brick using the build and welding parameters summarized in Table 2. The EBAM-W wire diameter is about 40% larger than the wires used for the other two processes and required 3.2 kW power (30kV at 105 mA), which is the highest of the three processes. In EBAM-W the wire cannot be coaxially located in order to avoid interference with the electron beam, and is instead fed into the melt pool from the side or directly in front of the beam. This wire feed orientation makes it more difficult to turn corners and reverse directions than with coaxial fed processes, and required a different scanning strategy. Fig. 3b shows the completed brick that was built on a 304L stainless steel substrate with 20 layers each approximately 2 mm high. The weld sequence used individual linear weld bead segments that were all made in the same direction and overlapped approximately 50% at 4.5 mm distance between beads.

The EBAM-W builds were made at a weld travel speed of 0.25 m/min, which is the slowest of the three processes. In this process, the beam was defocused 30 increments from sharp at a 250 mm work distance and was distributed over a several mm diameter using a deflection

pattern with nine concentric circles of one thousand points each. This pattern diffused the energy into a large enough area to facilitate the melting of the wire, and maintain the melt pool to provide the additive deposit. This method is common to the process, which seeks to deposit large volumes of material for the development of preforms that are then machined to final dimensional products. The brick was made with a maximum deposition rate of 1.2 kg/hr and was made at an energy per unit length of 750 J/mm. This energy per length of weld is approximately 2x that of the WAAM process and 10X that of the LAM-W. Owing to the nature of the deposit size, heat input, and lack of thermal cooling within a vacuum, the EBAM-W deposits will have the slowest cooling of the three processes, with corresponding changes to the microstructure.

Mechanical Testing and Characterization

Coupons were removed from each of the three bricks for mechanical property testing and microstructural characterization. The tensile samples were prepared by EDM extraction of blanks from the brick, followed by standard milling and turning to produce ASTM type round tensile bars as large as possible given the dimensions of the bricks. Since the bricks varied in size, different sized samples were produced with the dimensions given in Table 2. The largest sample was from the WAAM brick and measured 3 inch (76 mm) long, and had a 0.25 inch (6.4 mm) reduced diameter cross section as illustrated in Fig. 4a. The tensile bars were removed from three principal orientations of the brick as indicated in Fig. 4b, and labeled vertical (V) perpendicular to the layers, longitudinal (L) parallel to the weld direction, and transverse (T) which is the weld overlap direction perpendicular to L. The tensile bars were tested using servo-hydrolytic machines by each respective facility at room temperature and a strain rate of 1.5×10^{-3} /s. From these tests, yield strength, ultimate tensile strength, elastic modulus, and elongation to failure were measure and are reported in Table 2.

Additional characterization was performed on samples from each brick to measure residual ferrite, Vicker's microhardness, and Rockwell B macrohardness, as summarized in Table 2. All of the samples were metallographically prepared using standard cross sectioning and polishing methods, and etched electrolytically in an oxalic acid solution to revel the microstructural details. The delta ferrite was measured using a Magne-Gage and a No. 2 magnet with randomly spaced readings taken on the build cross section. Hardness measurements were made using calibrated testing machines, with the average of 8 or more samples per brick being reported. In addition, chemical composition of the builds were measured to see how they compared to the wire they were made from. Chemical analysis was performed on subsurface samples removed from the bricks using a calibrated LECO instruments to determine oxygen, nitrogen, carbon and sulphur content to better than 0.1ppm precision, while Inductively Coupled Plasma - Optical Emission Spectroscopy (ICP-OES) was used to measure the other elements.

Results

Laser Wire Additive Manufacturing

Macrostructures and microstructures of the LAM-W brick are shown in Fig. 5. An overall cross-sectional view of the entire 65 mm wide by 40 mm high brick is shown in Fig. 5a. This photograph shows the T-V plane that is perpendicular to the longitudinal weld direction. The faint boundaries of the 45 layers that make up the brick can be seen as horizontal lines, and the remnants of overlapping beads appear as crescent shapes that create a pattern that dips from the upper left to the lower right at an angle of approximately 25 deg. Superimposed on these patterns are columnar grain boundaries that trend upward, with the larger grains continuing through 10 or more layers. The columnar grains appear to be larger on the top surface of the brick than on the bottom, i.e., there appears to be a macroscopic growth of the columnar grains going on as additional layers are built on top of each other. Figure 5b shows a close up image of the macroscopic grain structure of the brick, where the above details of the individual overlapping beads and the columnar grains can be seen more closely.

A typical microstructure from this plane is shown in Fig. 5c at a much higher magnification. In this microstructure remnants of the dark etching delta ferrite dendrites are aligned vertically in the build direction, and have a primary dendrite arm spacing range of 6-8 micron. The resulting ferrite microstructure shows both vermicular and lacy morphologies as the result of primary ferrite solidification followed by partial transformation of the ferrite to austenite²². The residual ferrite content of the brick was measured to be 9.1 FN for the wire that had a Cr/Ni eq. ratio of 1.83, which is on the higher side, but in the range for welds made from 308L stainless steel wire. The oxygen content was measured to be 0.047 wt%, which is approximately 10x that of the starting material and is undesirable. The hardness values of the LAM-W brick of HRB=92.5 and HV=214 are typical for stainless steel welds²², and are higher than annealed 304L stainless steel minimum values of HRB=70 and HV=160.

Tensile bars were removed from the LAM-W brick along the transverse and longitudinal directions, but the brick was not tall enough to remove vertically oriented tensile bars. These samples were mechanically tested to failure, and a photograph of a typical broken tensile bar is shown in Fig. 6. The sample shows dimpling along the gage length, and the final fracture is a cup and cone type geometry. The stress-strain curves for the 308L LAM-W brick are shown in Fig. 7, and the tensile data are summarized in Table 2. These data indicate that the strongest orientation is in the transverse direction, where the average yield strength increased from 444 MPa (longitudinal) to 482 MPa (transverse). Similar results were obtained for the average ultimate strength that increased from 618 MPa (longitudinal) to 658 MPa (transverse). The average elongation values varied from 46.2% (transverse) to 47.7 (longitudinal). In addition to the tensile strength and elongation, the modulus of elasticity was highest in the transverse direction at 162 GPa as compared to the longitudinal direction at 133 GPa.

Wire Arc Additive Manufacturing

A cross sectional view of the entire 80 mm wide by 95 mm high brick is shown in Fig. 8a. This photograph is of the polished and etched surface and shows the T-V plane that is perpendicular to the longitudinal weld direction, just as was shown for the LAM-W brick. The faint boundaries of the overlapping individual weld beads are visible in each layer, and are significantly larger than those of the LAM-W sample. Figure 8b shows a close up image of the macroscopic grain structure of the brick, where the above details of the overlapping beads and the columnar grains can be seen more closely where individual grains can be seen growing upward in the remnants of each bead. One difference between the macrostructure of the WAAM part and the LAM-W part is that larger columnar grains appeared to grow through multiple layers of the LAM-W

A typical microstructure from this plane is shown in Fig. 8c at a much higher magnification from a region where weld beads are overlapping. Delta ferrite dendrites are aligned vertically in the build direction, and the ferrite microstructure shows both vermicular and lacy morphologies just as was observed in the LAM-W part, but with a larger primary dendrite arm spacing range of 18-25 microns. Other parameters that were measured are summarized in Table 2, including the residual ferrite content, micro and macro hardness and the oxygen content of the build. The residual ferrite content of the brick was measured to be 7.7 FN for the wire that had a Cr/Ni eq. ratio of 1.75, which are typical for welds made from 308L stainless steel wire. The oxygen content was measured to be 0.041 wt%, which is approximately 10x that of the starting material and is undesirable. The hardness values of the WAAM brick of HRB=88.2 and HV=206 are slightly lower than the LAM-W brick.

Tensile bars were removed from the WAAM brick along the transverse, longitudinal, and vertical directions and mechanically tested to failure. Figure 9 shows a photograph of a typical broken WAAM tensile sample. This sample has a rougher surface than the LAM-W tensile bar. Inhomogeneous deformation observed in the WAAM sample is the result of the large grains relative to the diameter of the tensile bar and will be discussed in more detail later. In addition, fine parallel wavy lines are clearly visible on the surface of the sample that is the result of slip bands forming in the large grains. The slip bands are more obvious in the WAAM sample than in the LAM-W sample, most like due to larger grains that are produced by WAAM than LAM-W. The stress-strain curves for the 308L WAAM brick are shown in Fig. 10 for each of the three orientations, and the tensile data are summarized in Table 2. These data show that the strongest orientation is in the transverse direction, and that the other two orientations were more than 10% weaker and similar to each other. The range of the average yield strengths varied from 323 MPa (vertical) to 382 MPa (transverse), while the range of the average ultimate strengths varied from 552 MPa (vertical) to 627 MPa (transverse). The average elongation values varied from 40.7% (transverse) to 51.9 (longitudinal). In addition to the tensile strength and elongation, the modulus of elasticity showed considerable variation among the different orientations. The modulus ranged from 162 to 212 GPa, and was highest in the transverse direction, while the other orientations averaged about 160 GPa.

Electron Beam Wire Additive Manufacturing

Macrostructures and microstructures of the EBAM-W brick are shown in Fig. 11. An overall cross sectional view of the entire 110 mm wide by 45 mm high brick is shown in Fig. 11a. This photograph is of the polished and etched surface and shows the T-V plane that is perpendicular to the longitudinal weld direction, just as was shown for the other bricks. There was some 90 deg. rotation of the weld beads required to make this brick, where the section shows both longitudinal and cross sectional boundaries of the welds. Columnar grains can be seen propagating from the bottom to the top of the brick. The faint boundaries of the overlapping individual weld beads are visible in each layer, and are significantly larger than those of the other bricks. Figure 11b shows a close up image of the macroscopic grain structure of the brick and individual weld bead boundaries.

A typical microstructure from the EBAM-W brick is shown in Fig. 11c at a much higher magnification. Delta ferrite dendrites are aligned vertically in the build direction, and the ferrite microstructure shows both vermicular and lacy morphologies just as was observed in the other bricks, but with a primary dendrite arm spacing range similar to the WAAM brick but slightly larger at 20-26 microns. Other parameters that were measured are summarized in Table 2, including the residual ferrite content, micro and macro hardness and the oxygen content of the build. The residual ferrite content of the brick was measured to be 4.9 FN for the wire that had a Cr/Ni eq. ratio of 1.73. This ferrite content is lower than would be expected for 308L SS and will be discussed in more detail later. The oxygen content was measured to be 0.0007 wt%, which is identical to that of the starting wire, and significantly lower than the other two processes. The hardness values of the EBAM-W brick of HRB=83.1 and HV=172.6 is the lowest of the three processes, but still harder than annealed 304L stainless steel.

Tensile bars were removed from the EBAM-W brick along the transverse, longitudinal, and vertical directions and mechanically tested to failure. Figure 12 shows a photograph of the necked region of a typical broken EBAM-W tensile sample. This sample looks similar to those of the other techniques, but the surface is even more dimpled where the large grains relative to the sample cross section create a lumpy appearance along the gage length and in the necked region of the tensile bar. As in the case with the WAAM sample, slip bands can be observed, but they are only obvious in the necked portion of the EBAM-W sample. The stress-strain curves for the EBAM-W brick are shown in Fig.13, and the tensile data are summarized in Table 2. These data show that the strongest orientation is again in the transverse direction. The range of the average yield strengths varied from 283 MPa (longitudinal) to 342 MPa (transverse), while the range of the average ultimate strengths varied from 529 MPa (vertical) to 584 MPa (transverse). The average elongation values varied from 46.3% (longitudinal) to 50.7 (vertical). In addition to the tensile strength and elongation, the modulus of elasticity also showed considerable variation. The modulus of the EBAM-W samples ranged from 158.5 to 220.6 GPa. The highest value of 220.6 GPa was in the transverse direction and very similar to the WAAM value of 212 GPa. The other two EBAM-W orientations averaged 165.4 GPa, which is also very similar to the WAAM build of 160 GPa.

Discussion

Microstructure

The three wire-based AM processing methods differ mainly in terms of travel speed of the weld and heat input per unit length of weld as summarized in Table 2. The LAM-W part was made at a travel speed of 1.2 m/min which is 3.8x faster than the WAAM part, and 4.8x faster than the EBAM-W part. Increasing travel speed influences the weld by reducing the overall size of the melt pool, elongating the melt pool length relative to its width, lowers the heat input per unit length of weld for a given power while increasing the cooling rate of the weld and refining the microstructure²³. When factoring in both the weld power and speed, the heat input per unit length was the lowest for LAM-W at 70 J/mm, while the WAAM was 5.3x higher, and EBAM-W was 10.7x that of the laser process. Based on this parameter alone, one would expect that the LAM-W would be quite different than the other two processes, and that WAAM and EBAM-W would be closer to each other. This appears to be true for the macrostructural features shown in Fig.5a,b, Fig.8a,b and Fig. 11a,b for laser, arc and electron beam respectively. In these figures, it is clear that the laser produced the smallest weld pool sizes and most refined microstructures. The approximate weld pool cross section sizes were measured and are summarized in Table 2 showing the large difference between the laser welds and the other two processes. The semicircular LAM-W weld pool measured approximately 3 mm wide and 1.0 mm deep with a cross sectional area of approximately 2.5 mm². The WAAM weld pool measured approximately 9 mm wide by 4.5 mm deep with a cross sectional area of approximately 25 mm², and had a deeper penetrating center region at the root of the weld and shallower near the weld toe than the laser weld. This weld cross section is sometimes referred to as finger penetration. The nearly semicircular EBAM-W weld pool measured approximately 10 mm wide by 6 mm deep and had a cross sectional area of approximately 45 mm², with slightly deeper penetration than a semicircular shape. In all cases these weld pool shapes were overlapped approximately 50% and penetrated approximately 50% of the weld width into the previous layer.

The microstructures at high magnification are shown in Fig. 5c, Fig. 8c and Fig.11c for laser, arc and electron beam respectively. Note the difference in magnifications used in these micrographs, where the laser is shown at higher magnification to bring out details of its finer structure. The microstructures are typical of welded 308L SS where the dendritic nature of solidification is clearly seen by the presence of the dark etching residual delta ferrite phase^{23 24}. The residual ferrite in the microstructure formed from ferrite dendrites solidifying as the primary phase with fully developed secondary arms for all three processes. The spacing of the primary and secondary arms is related to the cooling rate during solidification, where higher solidification rates produce smaller DAS sizes. The relationship between the microstructure scale and cooling rate during welding is represented by the following equation²³⁻²⁵:

$$\lambda = c (\varepsilon)^{-n} \quad (1)$$

In this equation, λ represents the dendrite arm spacing in microns, ε , is the cooling rate during solidification in K/s, C is a constant, and n is the cooling-rate exponent that can be found from the slope of a cooling rate vs. microstructural scale plot. The constants C and n are different for primary and secondary dendrite arms, and these constants are summarized in Table 3 using data from the literature for stainless steel alloys of similar composition²⁴. Table 3 also summarizes the primary and secondary DAS measurements for each of the processes, and from these measurements the estimated cooling rate range was calculated using eq. 1. Note that a range of DAS measurements are given that is observed in a single bead, where smaller spacings tend to appear on the bottom of the bead, and larger spacings towards the top.

These results show that LAM-W had the most refined microstructure with a primary DAS range of 6-8 microns and a secondary DAS range of 2.5-4 microns, which corresponds to a range of cooling rates from approximately 1,000 to 2,000 K/s depending on the measurement and location. WAAM had a coarser microstructure with a primary DAS range of 18-25 microns and a secondary DAS range of 7-9 microns, which corresponds to cooling rates less than 100K/s, i.e. more than one order of magnitude lower than LAM-W. EBAM-W had an even coarser microstructure with a primary DAS range of 20-26 microns and a secondary DAS range of 8-10 micron, which produced cooling rates less than that of WAAM and on the order of 50 K/s depending on measurement and location.

In addition to affecting the DAS and cooling rates, the different processes also had different ferrite contents, hardness values, and oxygen contents as summarized in Table 2. A complete chemical analysis for the samples, shown in Table 1, reveals that the composition of the all of the builds are close to the composition of the wire, except for oxygen content that was elevated approximately 6x relative to the starting wire for the WAAM and LAM-W processes, and would be considered to be out of specification for most applications⁹. Oxygen contents for the three wire-based builds show that only the EBAM-W has the same level of oxygen as the wire due to the superior vacuum conditions for this process, which is a big advantage of this process, particularly for refractory and other metals that are sensitive to oxygen or nitrogen pickup from the atmosphere.

The residual ferrite content of the weld is related its composition, specifically Cr/Ni equivalent ratio, and the cooling rate of the weld. Higher Cr/Ni ratios solidify with higher delta ferrite contents, and higher cooling rates tend to retain more of the delta ferrite since there is less time for solid state transformation of ferrite to austenite as the weld cools to room temperature^{23,24,26}. Although all of the processes used 308L SS wire, they were of slightly different composition as summarized in Table 1, and have different Cr/Ni ratios as calculated using the Suutala equivalents²⁷ as follows: $Cr_{eq} = Cr + 1.37Mo + 1.5Si + 2Nb + 3Ti$ and $Ni_{eq} = Ni + 0.31Mn + 22C + 14.2N + Cu$. The calculated Cr/Ni ratios of the wire are 1.83 for LAM-W, 1.75 for WAAM, and 1.73 for EBAM-W. The residual ferrite contents of the three builds are 9.1FN for LAM-W, 7.7FN for WAAM, and 4.9FN for EBAM-W. 308L SS weld compositions are designed to retain approximately 8FN ferrite to prevent solidification cracking during typical arc welding conditions, which is what was observed for the WAAM sample that has 7.7FN. The LAM-W sample had a higher ferrite content of 9.1FN, which is likely the result of both its higher Cr/Ni ratio and its higher cooling rate. The EBAM-W sample had a lower than typical ferrite

content for 308L SS of 4.9FN, which is most likely due to its slower cooling rate and subsequent phase transformations after solidification since its Cr/Ni ratio is typical for 308L SS. It is important to note that all of the samples showed primary ferrite solidification with no solidification cracking on the surface of the bricks or in microstructures observed in the cross sections.

Mechanical Behavior

The hardness values of the three different processes trend inversely with the heat input per unit length where the LAM-W sample had the highest hardness and the EBAM-W had the lowest hardness, as summarized in Table 2. The macrohardness values ranged from 83.1 HRB for EBAM-W to 92.5 HRB for LAM-W, while the microhardness values ranged from 172.6 HV for EBAM-W to 214 HV for LAM-W. The trends in hardness are what would be expected as the result of differing heat input on multiple factors including the scale of the microstructure, size of the columnar grains, presence of oxide inclusions, the amount of delta ferrite, and annealing that occurs more during the higher heat input welds. These effects will also influence other mechanical properties such as strength, ductility and toughness. The tensile properties of the bricks were measured in three different orientations relative to the build for each of the processes, and the results are summarized in Table 2 for yield and ultimate strengths, elongation to failure, and modulus of elasticity. These data are further shown in Fig. 14 that plots the four properties individually for each process and each orientation.

The yield strengths for each process are compared in Fig. 14a where the strength follows the same trend as the hardness for all orientations with LAM-W having the highest strength and EBAM-W having the lowest strength. The yield strength has a large range from 283 MPa to 482MPa, but all orientations and processes exceed the minimum yield strength of annealed 304L SS of 172 MPa, and in the case of LAM-W it was 2.8x higher. The ultimate tensile strengths for each process are compared in Fig. 14b, showing similar trends as the yield strength where LAM-W in the T orientation has the highest strength and EBAM-W in the L orientation has the lowest strength. The range of ultimate strengths varied from 528MPa to 658 MPa, which is smaller than the range of yield strengths. All of the orientations and processes exceeded the minimum ultimate strength of annealed 304L SS of 483 MPa, and in the case of LAM-W in the transverse orientation was 1.7x higher. The elongation to failure for each process are plotted in Fig. 14c that don't seem to follow a strong trend, but the lowest values tend to be for the T orientation and vary from 41.7% (WAAM, T) to 51.9% (WAAM, L). All elongations exceed the minimum for annealed 304L SS of 40%. The final figure, Fig. 14d, compares the modulus of elasticity for all orientations and processes, which had a very large range from 133.1 GPa to 220.6 GPa. This range of moduli spans the typical value of reported for polycrystalline annealed 304 SS of 193 GPa as the result of texture and is very similar to that observed in selective laser melting of 316 SS²⁸ that is created during the additive manufacturing.

Figure 15 shows close up photographs of the necked regions of the failed tensile bars from the WAAM brick for the transverse, longitudinal and vertical orientations. In terms of strength and ductility, the transverse orientation had the highest average yield strength of 382 MPa and the

lowest average elongation of 41.7%, whereas the other two orientations have elongations significantly higher at 51.6 and 51.9%. The visual appearance of the T and L samples are similar, both being in the same plane that is parallel with the build layer planes, but at 90 deg rotation from each other. The T-oriented sample appears to have larger facets than the L-oriented sample and does not neck down as much. The T-oriented sample failed at an approximate 45 deg angle across its face whereas the L-oriented sample failed in a cup and cone manner. The V-oriented sample has a different appearance, in that the grains are clearly elongating along the tensile axis, where elongated ridges form on the surface of the bar parallel to the tensile axis. The ridges curve to become more parallel with the tensile axis closer to the broken end where some necking is observed. It is believed that the V-oriented sample is showing the effects of the columnar grains which tend to grow in the vertical direction through multiple layers as observed in the macrophotograph of the WAAM brick cross section in Fig. 8a.

All of the tensile bar orientations show slip bands that appear to lie in planes largely perpendicular to the tensile axis. The band spacing is on the order of 100 microns with finer spacings on average observed in the V-orientation. Figure 16a shows a cross section through the center of one half of a broken tensile bar to illustrate the inhomogeneous deformation that occurs. This sample is from a longitudinal orientation and contains approximately 10 mm of a tapered region leading to the neck and final failure of the sample. The wavy surface is evidence of grains deforming at different rates, which can be seen more clearly in Fig.16b that is a higher magnification of the fractured end. Slip bands that intersect the surface of the tensile bar are shown in Fig. 16c in a region that etches darker than the surrounding areas, indicating higher localized deformation in the slip band region. Additional future work is planned to perform EBSD studies to characterize the grain orientations in the necked region of the tensile samples.

Texture and Anisotropy

The mechanical property data shows that all three processes produce properties that meet or exceed the minimum requirements for annealed 304L SS, which is the wrought equivalent of 308L SS, but that there are significant differences in the properties depending on the process and sample orientation. It is well known, that the elastic modulus, and other properties such as yield strength and thermal expansion, of a single crystal depend on its crystallographic orientation for metals and alloys such as stainless steels that are elastically anisotropic^{29 30 31}. These differences can be significant, and in the case of modulus, elastic anisotropy is known to vary by more than 3x for single crystal stainless steel alloys^{29 30}. Calculations³² using elastic constants from H. Ledbetter²⁹ show that the elastic modulus for austenitic stainless steels such as 308L will have the lowest value of 94GPa in the [100] direction, an average value of 193 GPa which would be expected in the [110] direction, and the highest value of 299 GPa in the [111] direction. In a polycrystalline sample this effect will not be as extreme, but can still vary considerably depending on the size of the grains and their degree of randomness. If the grains in the metal are randomly oriented in a large sample composed of many grains, the sample may appear to be isotropic as the crystallographic effects are averaged out. However if the grains

are large and non-random, i.e. textured, then the properties will be different in different orientations.

Figure 14d showed that sample orientation plays a role in the modulus of elasticity of the 308L SS wire-fed AM builds for all three wire-fed AM processes. The highest values were over 210 GPa in the transverse direction for WAAM and EBAM, while lower values were on the order of 160 GPa for the other orientations with the lowest values being for the LAM-W of 133.1 GPa in the L orientation. When compared to wrought 304L stainless steel the 308L SS AM bricks made from all three processes are clearly textured. The texture is related to the elongated columnar grains that form during solidification and tend to follow the [100] crystallographic direction³³. These grains curve and spiral into the weld pool as it solidifies depending on the weld pool shape^{34 35 36}, and are not oriented parallel to any one of the three principal directions of the brick (i.e. T,V, or L). In addition, epitaxial growth from multiple overlapping passes during a 3D build creates grain patterns that would not normally exist in single pass welds. Tensile bars removed from these complex microstructures have orientations that contain off-columnar axis components, which results in variations in the elastic modulus and in the mechanical properties different than the [100].

The elastic modulus values for all of the wire-based AM processes averaged 173 GPa, which is about 10% less than that of typical annealed wrought base metal. In all three processes the transverse orientation had a higher modulus than the other two orientations, and is higher than that of annealed wrought stainless steel by a considerable amount for the WAAM and EBAM-W processes. Based in the elastic modulus measurements it might be expected that the transverse orientation contains more grains closer to the [111] direction, and that the other two orientations contain grains closer to the [100] direction in order to give the measured range of modulus values observed. This can partially be explained in a qualitative sense by thinking about the overlapping weld beads that make up the AM bricks. Cross sections for each of the wire-fed bricks were shown in previous figures in the T-V plane, i.e., perpendicular to the welding direction, showing arc shaped remnants of previous weld beads that were partially remelted as new layers are added to the build. The arc shapes are present in a regular array created by the repeated parallel weld beads, and generate a macroscopic pattern that is also related to the grain texture. It is interesting to note that even though LAM-W, WAAM and EBAM-W are all made with different heat inputs per unit length and weld pool sizes, that all three processes show the transverse direction as having a higher elastic modulus. The LAM-W process however had lower modulus values than the other two, with both the L and T orientations being less than annealed polycrystalline 304 SS.

Figure 17 shows a schematic representation of the overlapping weld pools in an AM build to indicate how the macrostructure develops. The red highlighted region represents the portion of a weld bead that does not get remelted by subsequent passes, providing the substrate for other passes to solidify from, and leaving the bottom portion of the weld fusion line intact. Lines drawn in the weld beads indicate the general direction of heat flow and how, in this case, three different overlapping grains epitaxially grow from the one red highlighted bead. The orientation of dendrites and grains in the previous layer will intersect those growing along the heat flow direction of the new melt pool at different angles depending on where the weld pools overlap.

New dendrites and grains will grow epitaxially from the existing dendrites and grains and will attempt to orient themselves to the new heat flow direction, creating texture in the AM build. Although the 3D curved path that the grains follow in welds cannot be represented in a 2D cross section shown above, these views can be helpful to visualize how texture develops in the multipass AM builds. In other studies, the grain texture has been calculated in the fusion zone of single weld beads using a Monte Carlo code and coupled thermal fluids modeling. This model illustrates how dendrites and grains follow a curved path in as they grow along the maximum thermal gradient in a solidifying weld pool fusing a simplified 2-dimensional model of weld solidification³⁴, and a full 3-dimensional model of weld solidification^{35,36}. The path that the grains follow is a direct result of the weld pool shape and doesn't lie in a single plane except along the centerline of the weld. Therefore, none of the three principal orientations of the tensile bars will be composed of a single given crystallographic orientation, and will show some degree of texture depending upon how the [100] grains intersect the tensile axis.

Qualitative Comparison of the Three Wire-Fed Processes

The three processes each have advantages and disadvantages related to cost, ease of operation, microstructures that are produced, deposition rates, surface finish and mechanical properties. These aspects are important considerations when deciding on which process to use or invest in, and are highly specific to the final part being produced. Table 2 presented a detailed comparison of the processing parameters for each process and results obtained, indicating that LAM-W was made with the least energy per unit length, WAAM had an intermediate energy per unit length of weld of approximately 5x that of the laser process, and EBAM-W had the highest energy per unit length of weld at approximately 10x that of the laser process.

Many of the comparisons between the processes link back to the heat input factors in different ways, and Table 4 presents a qualitative comparison of the three processes where the different factors are indicated as low, L, medium, M, or high, H, based on the results of this study. This comparison is useful when considering tradeoffs for each process. For example if one needs a part fabricated at high deposition rates where surface finish a priority, then LAM-W would be a good choice based on its finer bead size and weld pool control. If cost per kg of material deposited is more important, then WAAM would be a good choice based on its high deposition rate, low operating and capital equipment cost, and low amount of energy per kg deposited. If chemical control of the final part is important and/or the part is being manufactured from reactive metals then EBAM would be the best choice based on its vacuum environment that eliminates the possibility of picking up unwanted contamination from the atmosphere.

In terms of mechanical properties of 308L SS, all processes produced properties that, when compared to annealed 304L SS, showed very favorable results. In all cases the yield strength, tensile strength and hardness exceeded that of annealed 304L SS, but there was a clear ranking in that the LAM-W process had the highest strengths and EBAM-W the lowest, largely the result of reduced heat input into the part and the more refined microstructure that it produces. The tensile ductility was not as sensitive to process, however there were mixed results depending on tensile sample orientation such that all of the processes had reasonable

ductility that exceeded the minimum for annealed 304 SS. This is a somewhat remarkable result in that the LAM-W process produced the strongest parts with no obvious loss in ductility compared to the other processes. Because of this LAM-W would be a good choice if increased strength is an important design factor. In terms of texture and the resulting anisotropic properties, all three processes showed a significantly high degree of texture based on microstructural observations, elastic moduli, and orientation dependent tensile strength properties. For each of the processes, the transverse tensile orientation had comparatively higher strengths than the other two orientations, which is a direct result of the solidification grain structure that forms during the layer by layer build.

Conclusions

In summary, the mechanical properties and microstructure of 308L stainless steel parts made by three different wire-based AM technologies were measured, and the following conclusions were made:

1. Best practice build parameters were developed for each wire-based AM process, resulting in significant differences between them. LAM-W used the highest speed, had the smallest weld pool, and had the lowest heat input per unit length of weld. WAAM used a medium speed and had a medium sized weld pool and had 5x the energy per length as the laser process. EBAM-W used the lowest speed, had the largest weld pool and had the highest energy per unit length of approximately 10x that of the laser process. However, when wire feed rate was factored in, the energy per kg of metal deposited only varied by 2.5x between the three processes with WAAM being the most efficient, and EBAM-W being the least efficient.
2. The differences in heat input between the three processes resulted in differences in the microstructure. LAM-W had the most refined microstructure as a result of its higher cooling rate during solidification, which was estimated to be on the order of 1,000K/s based on dendrite arm spacing measurements. Comparatively, WAAM and EBAM-W had less refined microstructures as a result of their slower cooling rates during solidification that were estimated to be less than 100K/s based on dendrite arm spacing measurements, with EBAM-W having the lowest cooling rates of the three processes.
3. Residual delta ferrite in the microstructure showed significant differences between the three processes. LAM-W and WAAM had the highest ferrite contents of 9.1FN and 7.7FN respectively, which are typical for 308L SS welds. EBAM-W had a ferrite content of 4.9FN, which is lower than expected for 308L SS. Since all three process solidified in the primary ferrite mode based on microstructural observations, the low ferrite content of EBAM-W is most likely due to its slow cooling rate through the ferrite to austenite solid state transformation temperature range, since typical electron beam single pass welds would not show a reduced ferrite content.

4. The composition of the parts built by each process was very similar to the starting wire composition except for the oxygen content. LAM-W and WAAM both picked up significant oxygen of 6x or greater than the wire composition. EBAM-W on the other hand showed no pickup of oxygen due to its superior vacuum conditions that are maintained during the build. Although the oxygen pickup by LAM-W and WAAM did not appear to adversely affect the mechanical properties of 308L SS it is important to note that this could be a concern when building parts out of oxygen sensitive metals or alloys.
5. The mechanical properties of the parts all exceeded the minimum values of annealed wrought 304L SS, however there were differences between the three processes. LAM-W had the highest ultimate strength, yield strength and hardness value, whereas EBAM-W had the lowest strength and hardness. These factors are a direct result of heat input and its effects on microstructure. Although the strengths were process dependent, the elongation to failure did not show any significant differences between the three processes.
6. Microstructural texture was observed in all of the parts as a result of the elongated columnar grains that form during solidification, combined with epitaxial growth from one layer to the next. The texture resulted in anisotropic properties in strength and elastic modulus. For a given process, the transverse orientation showed the highest strength and highest modulus, while the other two orientations, vertical and longitudinal, had properties similar to each other.
7. A comparison of the three processes shows relative advantages of each depending on the final application. For the parameters developed here, LAM-W demonstrated the best weld pool control and highest strength, making it useful when surface finish and mechanical properties are important. WAAM was the lowest cost process that produced the highest deposition rates with good resulting properties and surface finish, making it advantageous for larger parts. EBAM-W demonstrated the best control of the composition by preventing pickup of oxygen, making it useful for building parts out of atmosphere sensitive alloys.

Acknowledgments

The LLNL authors would like to thank John Sengthay, Cheryl Evans, and James Embree for metallography and hardness testing, Dave Urabe and Victor Hepa for tensile testing, and Dr. Jeff Florando for assistance with elastic modulus calculations. The AWE authors would like to thank Laserline GmbH, (Fraunhofer Straße 56218 Mülheim-Kärlich/Germany) for making the LAM-W 308L stainless steel component used in this investigation. The authors would also like to thank the people who helped with LANL EBAM research, development, and operations. Andy Duffield for Sciaky EBAM operation, Barry Bingham and Ruth Ann Vargas for procurement support, JJ O'Connor for facility Jeff Vigil and Jeff Robinson for machining of the tensile and metallography samples, JD Montalvo and Eric Tegmeier for metallography sample preparation and micrographs.

Auspices and Disclaimer

The LLNL portion of this work was performed under the auspices of the U.S. Department of Energy by Lawrence Livermore National Laboratory under Contract DE-AC52-07NA27344. This document was prepared as an account of work sponsored by an agency of the United States government. Neither the United States government nor Lawrence Livermore National Security, LLC, nor any of their employees makes any warranty, expressed or implied, or assumes any legal liability or responsibility for the accuracy, completeness, or usefulness of any information, apparatus, product, or process disclosed, or represents that its use would not infringe privately owned rights. Reference herein to any specific commercial product, process, or service by trade name, trademark, manufacturer, or otherwise does not necessarily constitute or imply its endorsement, recommendation, or favoring by the United States government or Lawrence Livermore National Security, LLC. The views and opinions of authors expressed herein do not necessarily state or reflect those of the United States government or Lawrence Livermore National Security, LLC, and shall not be used for advertising or product endorsement purposes.

Table 1: Compositions of the starting weld wire and the AM deposited builds in wt% for each of the three processes and calculated Cr and Ni equivalents from ²⁷.

Elements	LAM-W		WAAM		EBAM-W	
	Wire	Build	Wire	Build	Wire	Build
Ferrite Forming						
Cr	20.80	20.7	19.700	20.000	19.63	19.8
Mo	0.130	<0.01	0.200	0.110	0.07	0.10
Si	0.660	0.50	0.610	0.490	0.55	0.58
Ti	0.02	-	0.005	-	0.01	0.005
Nb	0.010	-	0.010	0.030	0.01	0.06
Austenite Forming						
Ni	10.20	10.1	10.400	10.600	10.34	10.7
Mn	1.650	1.61	1.540	1.530	1.82	0.58
C	0.021	0.020	0.021	0.023	0.017	0.024
N	0.061	0.060	0.037	0.040	0.023	0.027
Cu	0.020	0.02	0.090	0.110	0.31	0.08
Other						
O	0.005	0.047	0.007	0.041	-	0.002
P	0.009	0.011	0.019	0.024	0.027	0.027
S	0.012	0.013	0.022	0.020	0.014	0.016
Cr/Ni eq. Ratio						
Creq	22.01	21.46	20.92	20.95	20.55	20.94
Nieq	12.06	11.91	11.95	12.26	11.91	11.79
Cr/Ni eq	1.83	1.80	1.75	1.71	1.73	1.78

$$Cr_{eq} = Cr + 1.37Mo + 1.5Si + 2Nb + 3Ti, \quad Ni_{eq} = Ni + 0.31Mn + 22C + 14.2N + Cu$$

Table 2: Summary of all three wire-based AM build parameters and resulting properties.

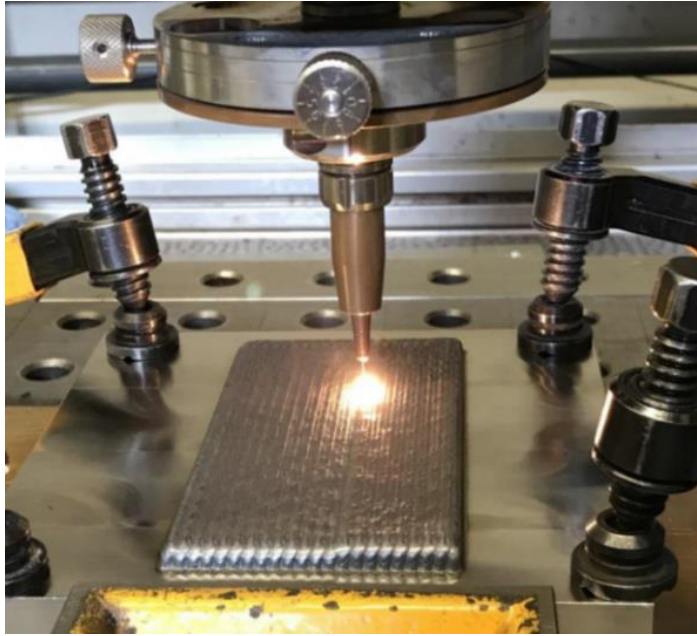
308-L SS wire Feed AM Results			LAM-W			WAAM			EBAM-W		
			No. Samples	Value	Stddev	No. Samples	Value	Stddev	No. Samples	Value	Stddev
Build and Weld Parameters	Heat Source Power	W		1400			1980			3150	
	Weld Speed	m/min		1.2			0.32			0.25	
	Energy/length of weld	J/mm		70			371			750	
	Wire Diameter	mm		1.1			1.1			1.5	
	Wire Speed	m/min		1.5			3.8			1.4	
	Max. Deposition Rate	kg/hr		0.7			1.7			1.2	
	Energy/amount deposited	J/gm		7463			4166			9675	
	Brick Size (LxWxH)	mm		115x65x40			130x80x95			110x110x45	
	Number of Layers			45			40			20	
	Layer height	mm		0.55			2.3			2.3	
	Bead Overlap	%		47			50			50	
	Weld Bead size (WxD)	mm		~3.0x1.0			~9x4.5			~10x6	
Weld cross section area	mm ²		~2.5			~25			~45		
Shielding gas			Argon			Ar-He-0.5%CO ₂			10 ⁻³ Torr vac.		
Build Properties	Microhardness	HV	15	214	9.4	19	205.6	9.1	14	172.6	13.6
	Macrohardness	HRB	6	92.5	2.3	8	88.2	1.3	12	83.1	2.2
	Ferrite Content	FN	12	9.1	0.22	8	7.7	0.23	15	4.9	0.8
	Primary dendrite arms	µm		6.0-8			18-25			20-26	
	Secondary dendrite arms			3.0-4			7.0-9			8.0-10	
	Oxygen content	wt%		0.047		3	0.041	0.002		0.002	
	Cr/Ni equivalent: wire/build	ratio		1.83			1.71			1.78	
Tensile Test Results	Gage Length	mm		16			25			16	
	Diameter	mm		4			6.4			3.18	
	Strain Rate	/s		1.5x10 ⁻³			1.5x10 ⁻³			1.0x10 ⁻³	
	Extensometer Length	mm		12.5			25			12.5	
Vertical	Yield Stress	Mpa				3	323.4	18.2	3	308.9	7
	UTS	MPa				3	551.6	3.1	3	528.8	14
	Modulus (0.1%)	Gpa				3	166.2	9.6		172.4	
	Elongation to failure	%				3	51.6	12.7	3	50.7	6
Longitudinal	Yield Stress	Mpa	14	444.0	6.6	4	343.4	15.7	7	283.4	21
	UTS	MPa	14	617.8	7.5	4	570.9	8.1	7	565.4	14
	Modulus (0.1%)	Gpa	14	133.1	8.8	4	162.0	9.3		158.5	
	Elongation to failure	%	14	47.7	2.7	4	51.9	2.3	7	46.3	4
Transverse	Yield Stress	Mpa	8	482.0	17.3	4	382.0	3.8	7	342.0	41
	UTS	MPa	8	657.8	12.1	4	626.8	19.0	7	584.0	28
	Modulus (0.1%)	Gpa	8	162.0	12.1	4	211.7	22.2		220.6	
	Elongation to failure	%	8	46.2	8.1	4	41.7	2.7	7	49.6	5

Table 3: Summary of dendrite arm spacing (DAS) and estimated cooling rates for each of the three processes. The range of dendrite arm spacing is within an individual weld bead.

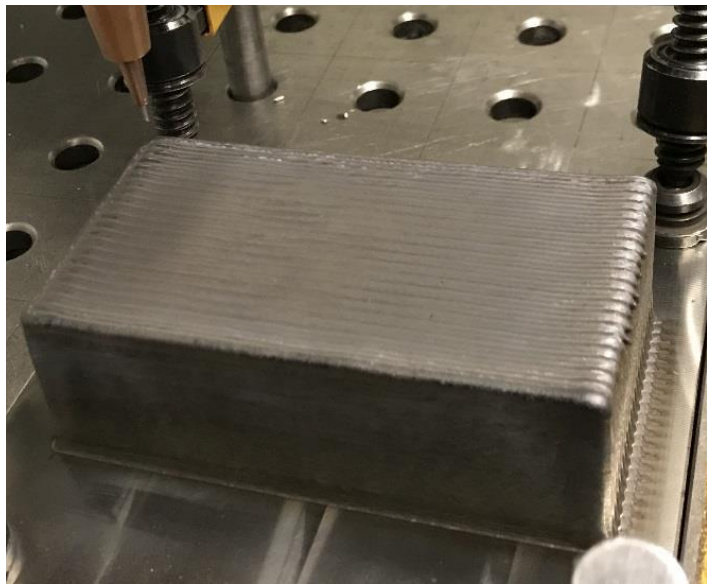
Process	Feature	DAS Constants for eq. 1	Spacing Range	Cooling Rate Range
		(C / n)	(μm)	(K/s)
LAM-W	Primary DAS	80 / 0.33	6-8	1070-2560
	Secondary DAS	25 / 0.28	3-4	695-1940
WAAM	Primary DAS	80 / 0.33	19-25	34-78
	Secondary DAS	25 / 0.28	7-9	38-94
EBAM-W	Primary DAS	80 / 0.33	20-26	30-66
	Secondary DAS	25 / 0.28	8-10	26-58

Table 4: Qualitative comparison of the three wire-based AM processes.

Property	LAM-W	WAAM	EBAM-W
Cost of equipment	M	L	H
Cost of operation	M	L	H
Deposition Rate	L	H	M
Weld pool size	L	M	H
Surface Finish	H	M	L
Weld Speed	H	M	L
Energy/unit length	L	M	H
Energy/kg deposited	M	L	H
Dendrite spacing	L	M	H
Cooling Rate	H	M	L
Yield Strength	H	M	L
Ultimate Strength	H	M	L
Hardness	H	M	L
Elongation	M	M	M
Atmosphere control	L	L	H
Oxygen pickup	H	H	L
Grain texture effects	M	H	H

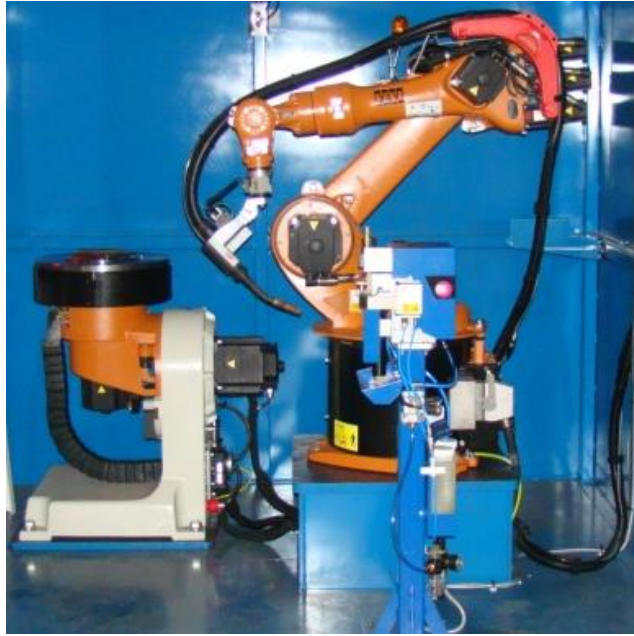


(a)

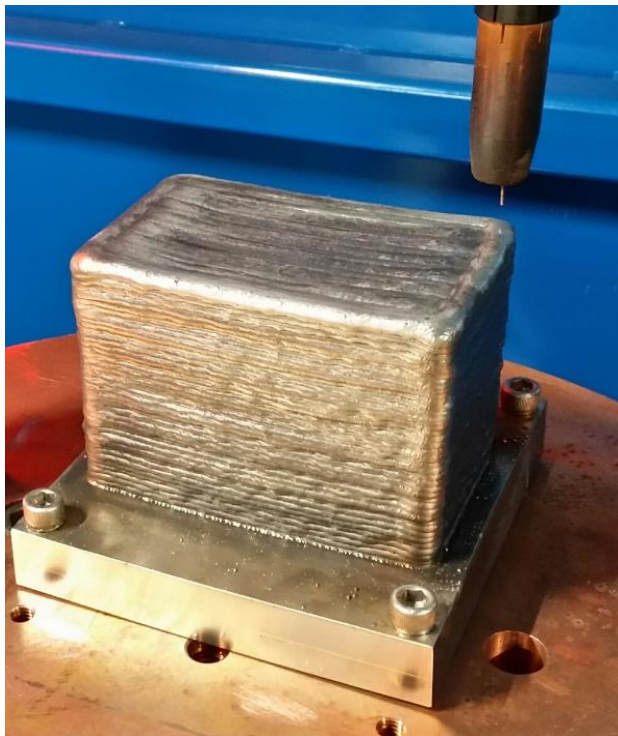


(b)

Figure 1: Photographs of the LAM-W process showing: a) the system during the build, and b) the final LAM-W brick.



(a)



(b)

Figure 2: a) 8-axis WAAM cell with Fronius GMAW wire feed, power supply and torch, and b) completed solid WAAM brick made from 308L stainless steel wire.

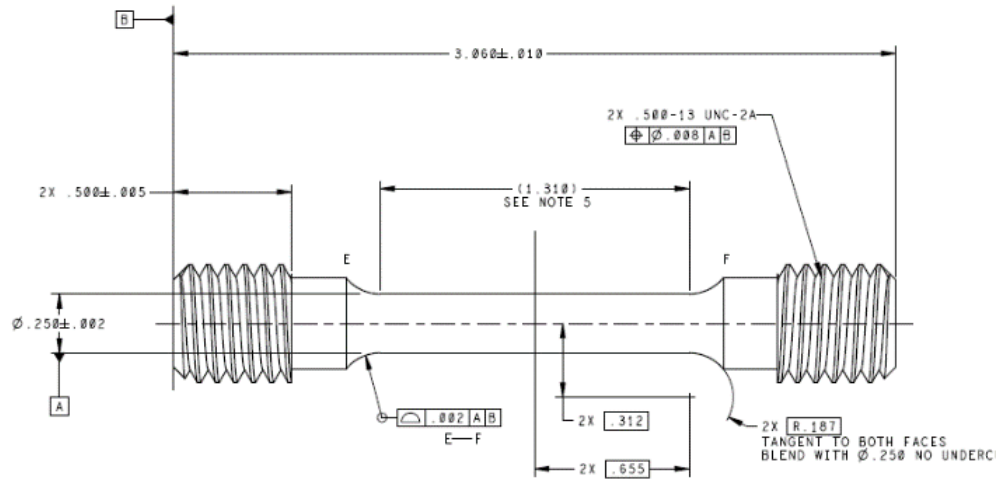


(a)

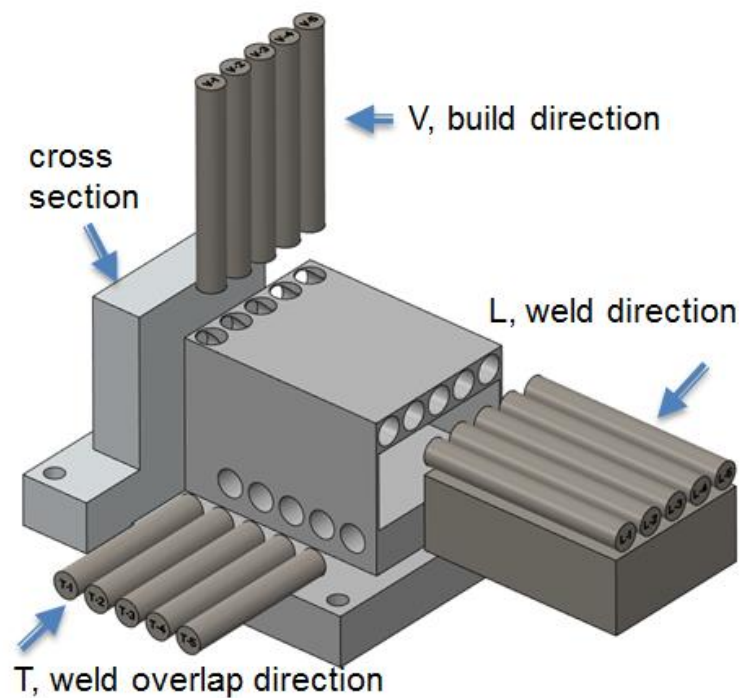


(b)

Figure 3: a) Photograph of the vacuum chamber, gun and wire feeder of the EBAM-W system, and b) image of 308L EBAM-W build with blanks cut out for tensile samples.

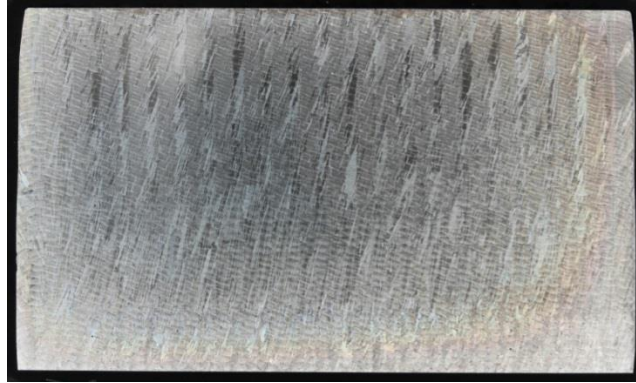


(a)

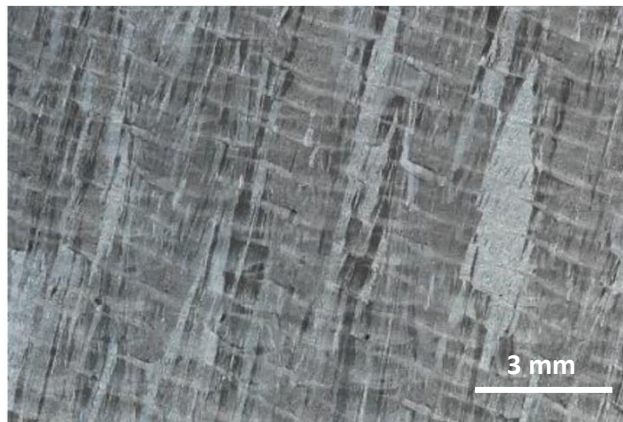


(b)

Figure 4: a) Tensile bar configuration from WAAM brick (dimensions in inches), which is similar to the other tensile bars but larger in size, and b) tensile bar orientation relative to the brick dimensions.



(a)



(b)



(c)

Fig 5: LAM-W microstructures from laser line: a) photograph of the polished and etched 115 mm wide cross section, b) photograph of the weld bead and grain structure detail, and c) residual delta ferrite microstructure at high magnification.

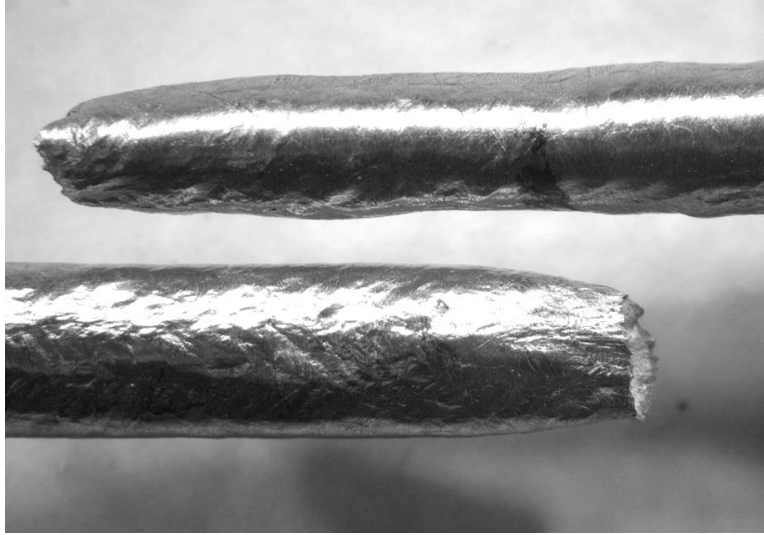


Fig 6: Photograph of a failed LAM-W tensile bar showing a dimpled surface along the in the gage length of the sample.

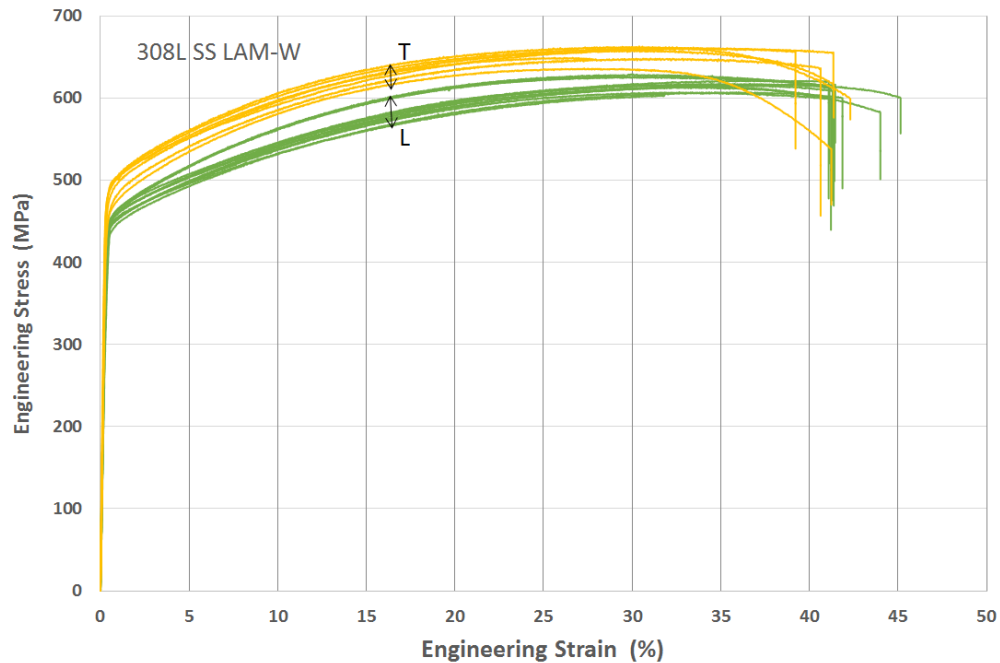
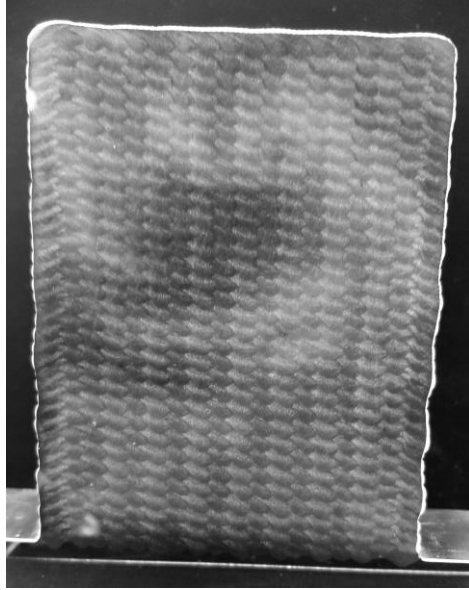
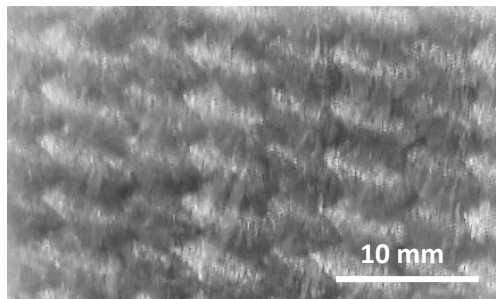


Fig 7: LAM-W tensile test results for the transverse (T) and longitudinal (L) orientations, showing the transverse orientation to have the highest yield and ultimate strengths.



(a)



(b)



(c)

Figure 8: WAAM microstructures: a) photograph of polished and etched 80 mm wide cross section of the brick, b) photograph of the weld bead and grain structure detail, and c) residual delta ferrite microstructure at high magnification.



Figure 9: Photograph of a failed WAAM tensile bar showing the effects of large grains creating a dimpled surface in the gage length and at the necked region on the sample.

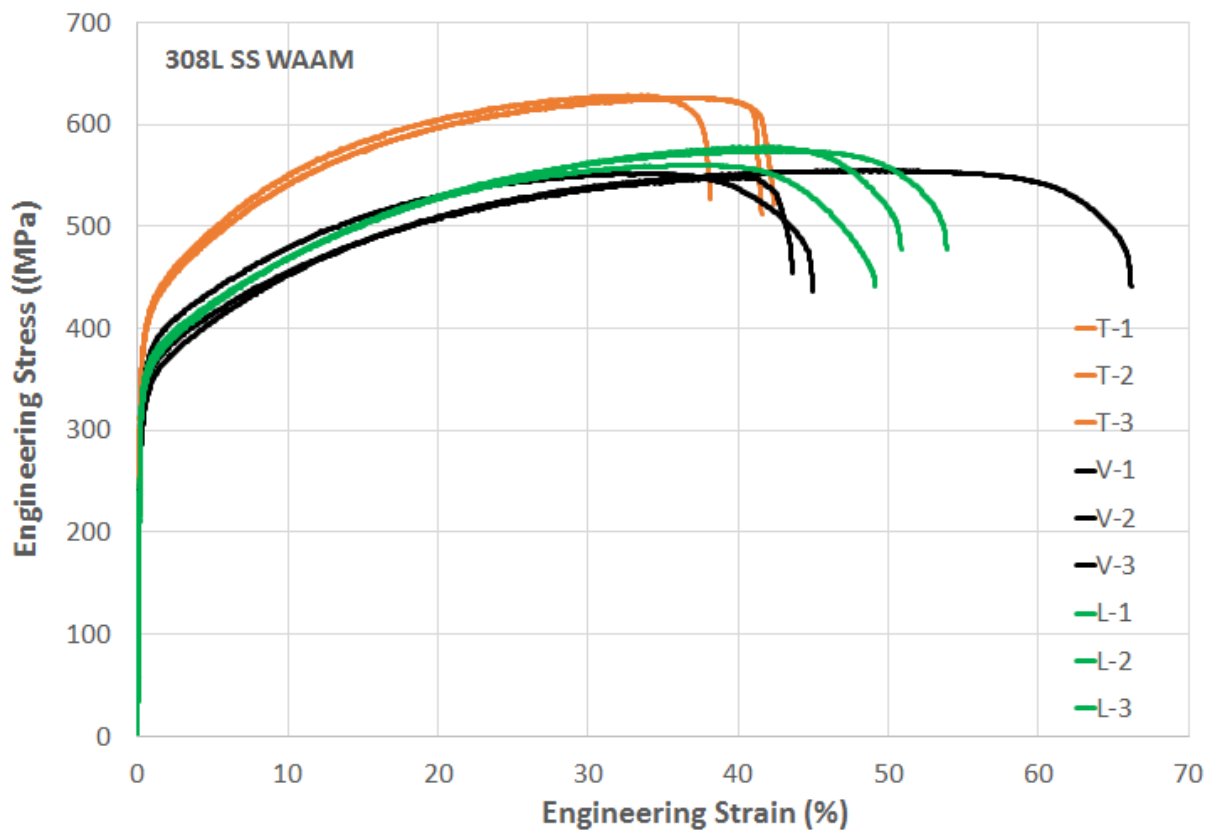
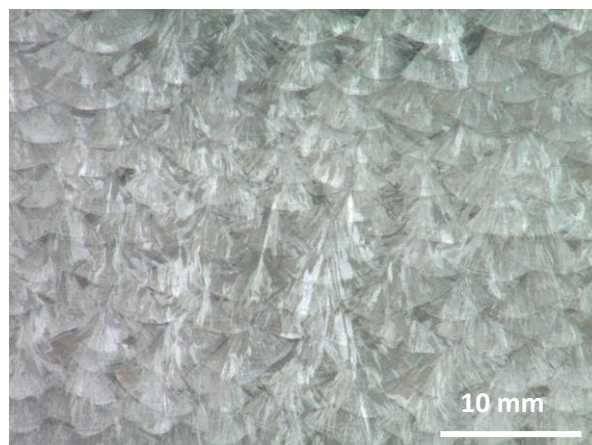


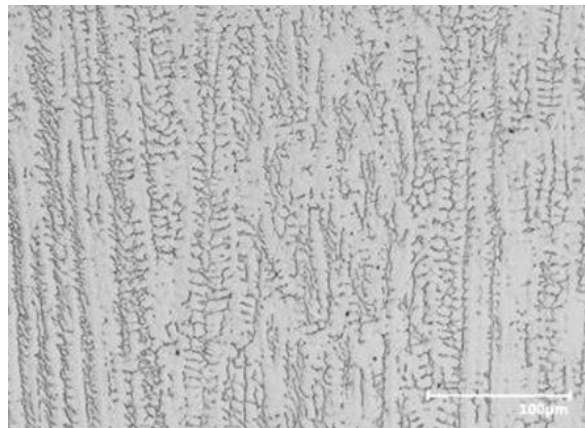
Figure 10: WAAM tensile results for the three orientations, showing the transverse direction (T) to have the highest yield and ultimate strength.



(a)



(b)



(c)

Fig 11: EBAM-W microstructures: a) photograph of the polished and etched 110 mm wide brick cross section with 1 cm background markings, b) photograph of the weld bead and grain structure detail, and c) residual delta ferrite microstructure at high magnification.



Figure 12: Photograph of a failed EBAM-W tensile bar showing the effects of large grains creating a lumpy surface throughout the entire gage length

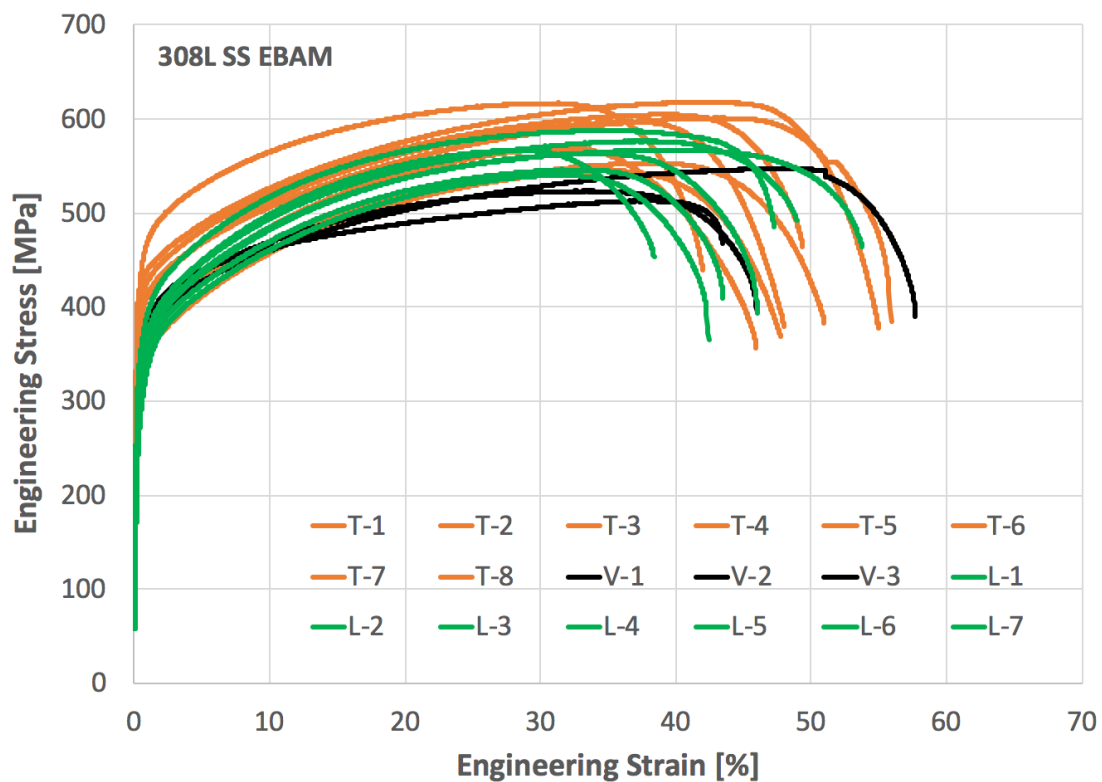


Figure 13: EBAM-W tensile test results for the transverse (Y), longitudinal (X), and vertical (Z) orientations.

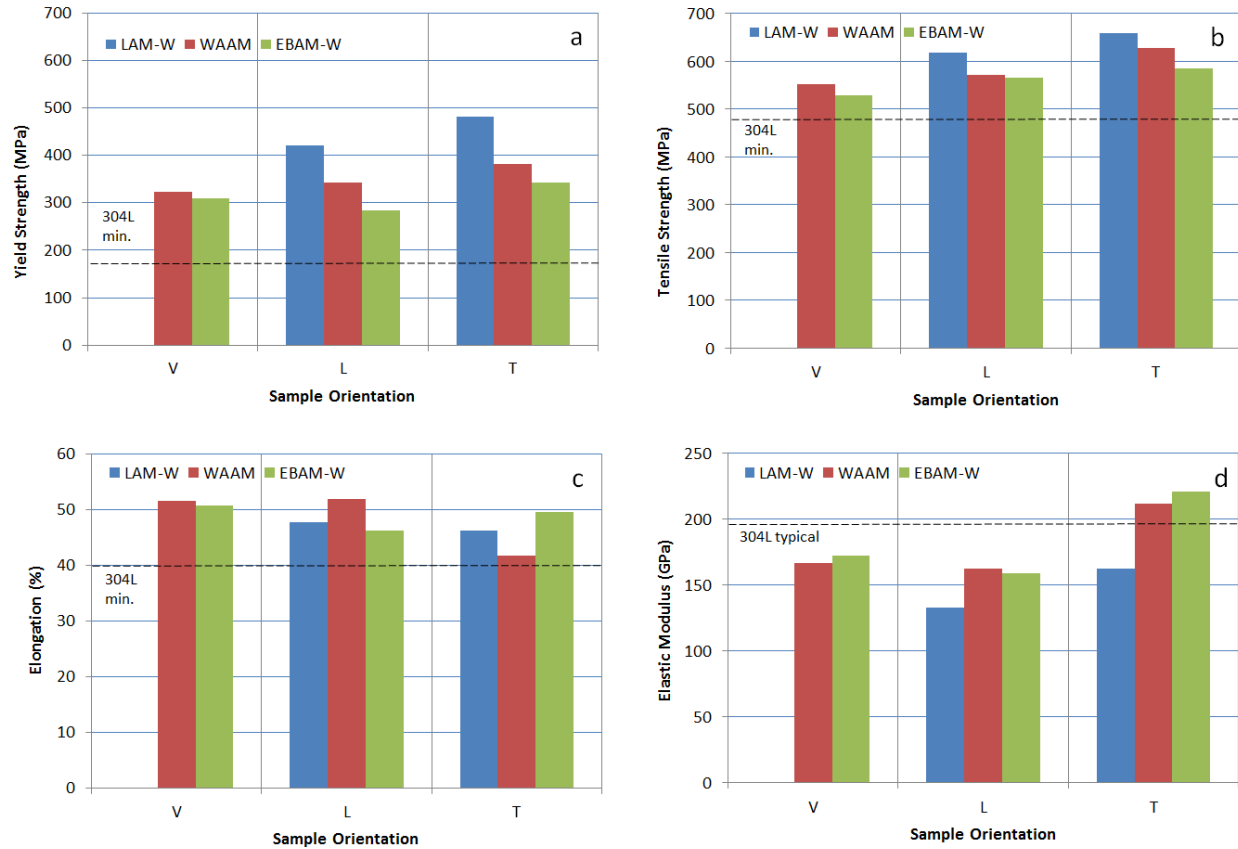


Figure 14: Summary of the mechanical property tests for each AM process as a function of sample orientation. The horizontal dashed lines correspond to properties of annealed 304L stainless steel.

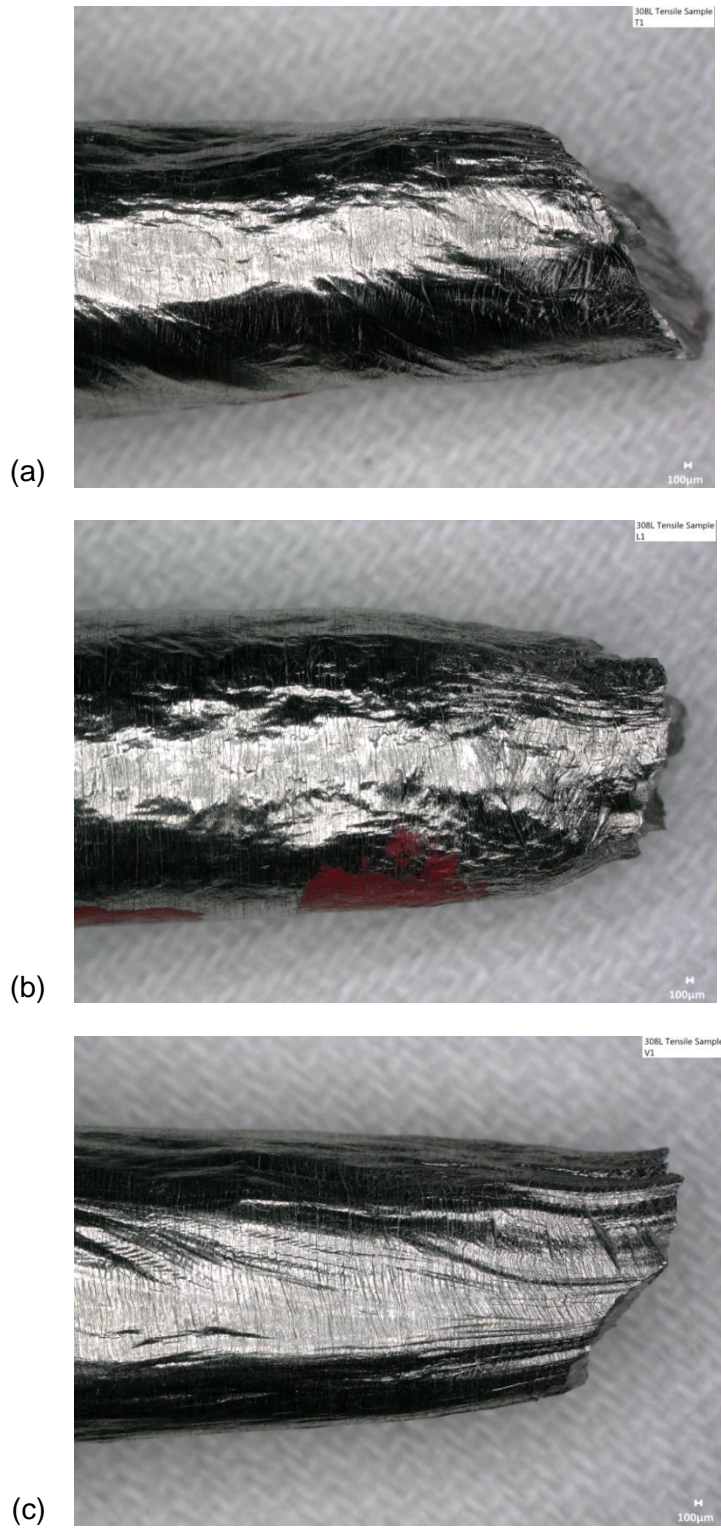


Figure 15: Comparison of the necked regions of the failed tensile bars from the WAAM brick for a) transverse direction, b) longitudinal direction, and c) vertical orientations.

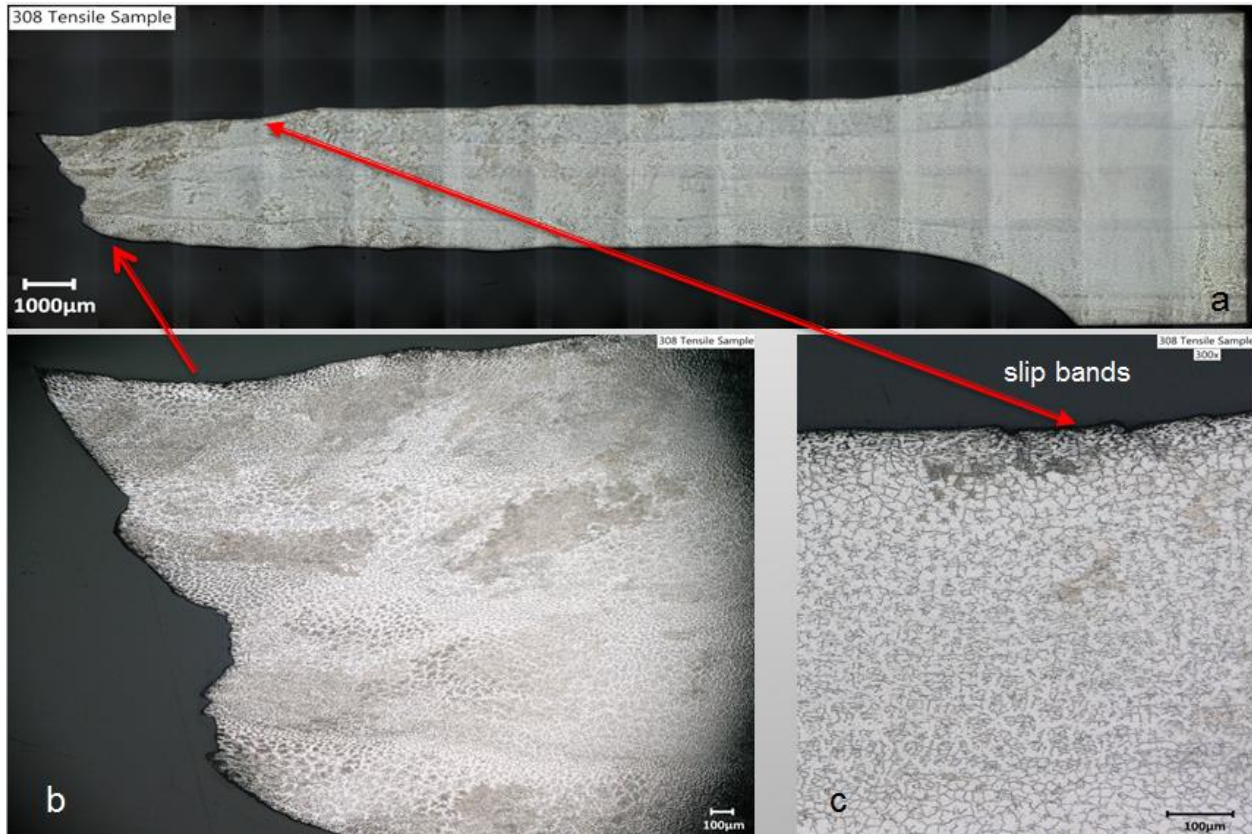


Figure 16: a) Cross section through the center of a broken tensile bar, b) higher magnification detail near the fracture surface, and c) higher magnification detail in the necked portion of the gage length.

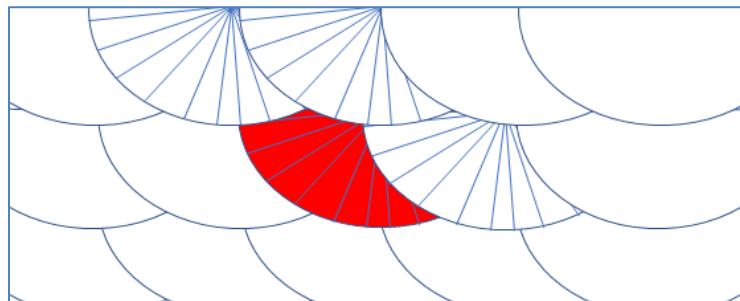


Figure 17: Schematic representation of overlapping weld pools in an AM build. The red highlighted region represents the portion of a weld bead that does not get remelted by subsequent passes, providing the substrate for other passes to solidify from.

References

- 1 DebRoy, T. *et al.* Additive manufacturing of metallic components – Process, structure and properties. *Progress in Materials Science* **92**, 112-224, doi:10.1016/j.pmatsci.2017.10.001 (2018).
- 2 Sames, W. J., List, F. A., Pannala, S., Dehoff, R. R. & Babu, S. S. The metallurgy and processing science of metal additive manufacturing. *International Materials Reviews* **61**, 315-360, doi:10.1080/09506608.2015.1116649 (2016).
- 3 Milewski, J. O. *Additive Manufacturing of Metals: From Fundamental Technology to Rocket Nozzles, Medical Implants, and Custom Jewelry*. (Springer International Publishing, 2017).
- 4 Ding, D., Pan, Z., Cuiuri, D. & Li, H. Wire-feed additive manufacturing of metal components: technologies, developments and future interests. *The International Journal of Advanced Manufacturing Technology* **81**, 465-481, doi:10.1007/s00170-015-7077-3 (2015).
- 5 DebRoy, T., *et al.*, . Scientific, technological and economic issues in metal printing and their solutions. *Nature Materials* **18**, doi: 10.1038/s41563-019-0408-2 (2019).
- 6 EBAM® is a trademark of Sciaky, Inc., Chicago, IL USA.
- 7 Block-Bolten, A. & Eagar, T. W. Metal vaporization from weld pools. *Metallurgical Transactions B* **15**, 461-469, doi:10.1007/bf02657376 (1984).
- 8 Bermingham, M. J., Thomson-Larkins, J., St John, D. H. & Dargusch, M. S. Sensitivity of Ti-6Al-4V components to oxidation during out of chamber Wire + Arc Additive Manufacturing. *Journal of Materials Processing Technology* **258**, 29-37, doi:10.1016/j.jmatprotec.2018.03.014 (2018).
- 9 Elmer, J. W., and Gibbs, G. The Effect of Atmosphere on the Composition of Wire Arc Additive Manufactured Metal Components *Science and Technology of Welding and Joining, Special Issue on Additive Manufacturing and 3D Printing* **24**, 367-374, doi:10.1080/13621718.2019.1605473 (2019).
- 10 Demir, A. G. Micro laser metal wire deposition for additive manufacturing of thin-walled structures. *Optics and Lasers in Engineering* **100**, 9-17, doi:<https://doi.org/10.1016/j.optlaseng.2017.07.003> (2018).
- 11 Baufeld, B., Brandl, E. & van der Biest, O. Wire based additive layer manufacturing: Comparison of microstructure and mechanical properties of Ti–6Al–4V components fabricated by laser-beam deposition and shaped metal deposition. *Journal of Materials Processing Technology* **211**, 1146-1158, doi:<https://doi.org/10.1016/j.jmatprotec.2011.01.018> (2011).
- 12 Brandl, E., Schoberth, A. & Leyens, C. Morphology, microstructure, and hardness of titanium (Ti-6Al-4V) blocks deposited by wire-feed additive layer manufacturing (ALM). *Materials Science and Engineering: A* **532**, 295-307, doi:<https://doi.org/10.1016/j.msea.2011.10.095> (2012).
- 13 Fu, J. *et al.* Microstructure and Mechanical Properties of Ti-6Al-4V Fabricated by Vertical Wire Feeding with Axisymmetric Multi-Laser Source. *Applied Sciences* **7**, 227 (2017).
- 14 Henri, P. *et al.* Laser cladding with coaxial wire feeding. *International Congress on Applications of Lasers & Electro-Optics* **2012**, 1196-1201, doi:10.2351/1.5062408 (2012).
- 15 Brandl, E., Leyens, C. & Palm, F. Mechanical Properties of Additive Manufactured Ti-6Al-4V Using Wire and Powder Based Processes. *IOP Conference Series: Materials Science and Engineering* **26**, 012004, doi:10.1088/1757-899x/26/1/012004 (2011).
- 16 Martina, F., Mehnen, J., Williams, S. W., Colegrove, P. & Wang, F. Investigation of the benefits of plasma deposition for the additive layer manufacture of Ti–6Al–4V. *Journal of Materials Processing Technology* **212**, 1377-1386, doi:10.1016/j.jmatprotec.2012.02.002 (2012).
- 17 Martina, F., Colegrove, P. A., Williams, S. W. & Meyer, J. Microstructure of Interpass Rolled Wire + Arc Additive Manufacturing Ti-6Al-4V Components. *Metallurgical and Materials Transactions A* **46**, 6103-6118, doi:10.1007/s11661-015-3172-1 (2015).

- 18 Ho, A. *et al.* On the origin of microstructural banding in Ti-6Al4V wire-arc based high deposition rate additive manufacturing. *Acta Materialia* **166**, 306-323, doi:10.1016/j.actamat.2018.12.038 (2019).
- 19 Gockel, J., Fox, J., Beuth, J. & Hafley, R. Integrated melt pool and microstructure control for Ti-6Al-4V thin wall additive manufacturing. *Materials Science and Technology* **31**, 912-916, doi:10.1179/1743284714y.0000000704 (2015).
- 20 Fuchs, J., Schneider, C. & Enzinger, N. Wire-based additive manufacturing using an electron beam as heat source. *Welding in the World* **62**, 267-275, doi:10.1007/s40194-017-0537-7 (2018).
- 21 Vaja, J. LaserLine GmbH, Fraunhofer Strasse, 56218 Mulheim-Karlich, Germany. (2018).
- 22 Elmer, J. W., Ellsworth, G. F., Florando, J. N., Golosker, I. V. & Mulay, R. P. Microstructure and Mechanical Properties of 21-6-9 Stainless Steel Electron Beam Welds. *Metallurgical and Materials Transactions A* **48**, 1771-1787, doi:10.1007/s11661-017-3996-y (2017).
- 23 Kou, S. *Welding Metallurgy*. second edition edn, (Wiley-Interscience, 2002).
- 24 Elmer, J. W., Allen, S. M. & Eagar, T. W. Microstructural development during solidification of stainless steel alloys. *Metallurgical Transactions A* **20**, 2117-2131, doi:10.1007/bf02650298 (1989).
- 25 Katayama, S., Matsunawa, A. Solidification Microstructure of Laser Welded Stainless Steels. *Proc. ICALEO 1984*, 60-67 (1985).
- 26 Zhang, W., DebRoy, T., Palmer, Elmer, JW. Modeling of Ferrite Formation in a Duplex Stainless Steel Weld Considering Non-uniform Starting Microstructure. *Acta Materialia* **53**, doi: 10.1016/j.actamat.2005.05.040 (2005).
- 27 Suutala, N. EFFECT OF SOLIDIFICATION CONDITIONS ON THE SOLIDIFICATION MODE IN AUSTENITIC STAINLESS-STEELS. *Metallurgical Transactions a-Physical Metallurgy and Materials Science* **14**, 191-197, doi:10.1007/bf02651615 (1983).
- 28 Hitzler, L. *et al.* On the Anisotropic Mechanical Properties of Selective Laser-Melted Stainless Steel. *Materials* **10**, 1136 (2017).
- 29 Ledbetter, H. Monocrystal-Polycrystal Elastic Constants of a Stainless Steel. *physica_status_solidi_A*, 85-89 (1984).
- 30 Kikuchi, M. ELASTIC ANISOTROPY AND ITS TEMPERATURE DEPENDENCE OF SINGLE-CRYSTALS AND POLYCRYSTAL OF 18-12 TYPE STAINLESS-STEEL. *Transactions of the Japan Institute of Metals* **12**, 417-&, doi:10.2320/matertrans1960.12.417 (1971).
- 31 Dewey, B. R., Adler, L., King, R. T. & Cook, K. V. Measurements of anisotropic elastic constants of type 308 stainless-steel electroslag welds. *Experimental Mechanics* **17**, 420-426, doi:10.1007/bf02324239 (1977).
- 32 Florando, J. N., and Elmer, J. W. . Unpublished work, Lawrence Livermore National Laboratory. (2018).
- 33 Kurz, W. *Fundamentals of Solidification*. (Trans Tech Publications, 1986).
- 34 Wei, H. L., Elmer, J. W. & DebRoy, T. Origin of grain orientation during solidification of an aluminum alloy. *Acta Materialia* **115**, 123-131, doi:<https://doi.org/10.1016/j.actamat.2016.05.057> (2016).
- 35 Wei, H. L., Elmer, J. W., and DebRoy, T. Three-dimensional modeling of grain structure evolution during welding of an aluminum alloy. *Acta Materialia* **126**, 413-425, doi:10.1016/j.actamat.2016.12.073 (2017).
- 36 Wei, H. L., Elmer, J. W., and DebRoy, T. & DebRoy, T. Crystal growth during keyhole mode laser welding. *Acta Materialia* **133**, 10-20, doi:10.1016/j.actamat.2017.04.074 (2017).